# Dual-vortex plasmatron: a novel plasma source for $CO_2$ conversion

G. Trenchev and A. Bogaerts

Research group PLASMANT, Department of Chemistry, University of Antwerp, Universiteitsplein 1, B-2610 Antwerp, Belgium

**Abstract.** Atmospheric pressure gliding arc (GA) discharges are gaining increasing interest for $CO_2$ conversion and other gas conversion applications, due to their simplicity and high energy efficiency. However, they are characterized by some drawbacks, such as non-uniform gas treatment, limiting the conversion, as well as the development of a hot cathode spot, resulting in severe electrode degradation. In this work, we built a dual-vortex plasmatron, which is a GA plasma reactor with innovative electrode configuration, to solve the above problems. The design aims to improve the $CO_2$ conversion capability of the GA reactor by elongating the arc in two directions, to increase the residence time of the gas inside the arc, and to actively cool the cathode spot by rotation of the arc and gas convection. The measured $CO_2$ conversion and corresponding energy efficiency indeed look very promising. In addition, we developed a fluid dynamics non-thermal plasma model with argon chemistry, to study the arc behaviour in the reactor and to explain the experimental results.

## 1. Introduction

Atmospheric pressure plasma reactors have received significant recognition in the field of plasma-assisted gas conversion, and more specifically for $CO_2$ conversion into value-added compounds [1–3] Most studies have been performed with microwave (MW) plasma [4–6], dielectric barrier discharge (DBD) [7,8], atmospheric pressure glow discharge (APGD) [9] and gliding arc (GA) reactors [10,11]. While their application has been generally successful, every reactor type comes with a set of specific drawbacks, and the performance can vary significantly from setup to setup.

For instance, MW plasma reactors show good energy efficiency (above 50% for $CO_2$ conversion), but only at specific conditions, such as reduced pressure or vortex flow design [3,6]. DBD reactors are able to operate at atmospheric pressure and show relatively high CO2 conversion (up to 30% and more), but at very limited energy efficiency (up to 10%) [3]. Recently, certain advances have been made with APGD reactors, with an improved conversion-efficiency balance [9], although the energy efficiency was limited to 25-30% due to the plasma contacting the reactor walls, which leads to heat losses.

A classical GA typically consists of two blade-shaped opposing electrodes, between which a high voltage is applied [12,13]. Gas flow is supplied at the base of the electrodes. When the voltage is high enough, an electrical discharge is initiated at the shortest distance between the electrodes, upon which the electrical current increases, and the voltage drops. The arc discharge then glides upwards, driven by natural buoyancy and the gas flow velocity. Upon reaching a point where the discharge power is insufficient to maintain the discharge, the arc disintegrates, shifting the voltage to a high level again, and a new arc is initiated at the reactor base.

GA reactors have shown promising performance in $CO_2$ conversion, with energy efficiency around 25-30%, but conversion limited to 8-9% [14–16], due to the limited fraction of gas passing through the arc. Moreover, they suffer from problematic electrode degradation, and significant convective heat losses [17]. The reverse-vortex GA reactor, also called GA plasmatron (GAP), was developed at Drexel University to overcome these problems [10]. It utilizes a reverse-vortex principle to insulate the discharge and reduce the heat losses towards the reactor walls. Despite its advantages, the $CO_2$ conversion is still limited to 8-9%, for an energy efficiency of 25-30% [11]. This has also been attributed to the limited amount of gas actually passing through the discharge zone [18]. Furthermore, a hot cathode spot is formed, which shifts the discharge regime close to thermal equilibrium. Indeed, the temperature of this cathode spot was measured to reach values of 6000 K or more [19]. The most energy-

efficient $CO_2$ dissociation, however, occurs by vibrational excitation, but a strong vibrational population only occurs when there is a clear vibrational-translational non-equilibrium, i.e., at lower gas temperature [1], [2], [3].

In this work, we designed and tested a novel GA reactor, based on our insights obtained from reverse-vortex flow GA reactors[11,18,20]. More specifically, we developed a dual-vortex electrode configuration, supported by fluid dynamics and plasma simulations. This novel design aims to improve the $CO_2$ conversion capability of the reactor by elongating the arc in two directions, in order to increase the residence time, as well as by diffusing the arc with a highly turbulent flow. Furthermore, the design seeks to actively cool the cathode spot, by rotating it along the electrode surface with strong convectional cooling. We also developed a fluid dynamics non-thermal plasma model to study the arc behaviour in the reactor.

## 2. Existing reverse-vortex flow GA reactor: concept and limitations

Reverse-vortex flow stabilization is a known method for gaseous flame and plasma stabilization [1,21,22], and it has been practically implemented in a GA reactor, for gas conversion applications[10]. As shown in figure 1 (a), such a reactor is essentially composed of a tubular vessel (at cathode potential) with tangential inlets. As shown in the figure, this forms a forward vortex flow (black spiral) that creeps along the reactor walls, and upon reaching the bottom of the reactor, it forms an inner vortex (in red) with a smaller radius, travelling in the opposite direction (hence reverse-vortex), after which the gas leaves the reactor through the axial outlet (at anode potential). In simple terms, mass flow is directed from the walls to the reactor centre, which effectively insulates the walls from convective heating. The number of inlets may vary (e.g. 1-6). In [23] we developed a model for a conceptual reverse-vortex flow GA reactor with 4 inlets, while in [18], we considered 6 inlets, like in the actual reverse-vortex flow GA reactor – also called GAP – developed at Drexel University [10]. The outlet diameter can vary, but generally it should be significantly smaller than the diameter of the reactor itself, to avoid that the gas, when entering the reactor, can immediately escape without traveling through the entire arc, and hence to maximize the reverse-vortex flow concept [1].
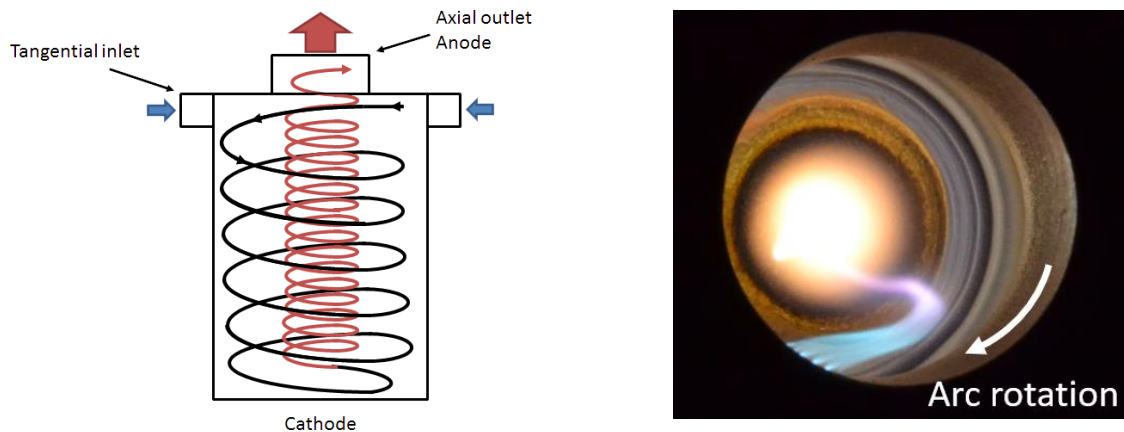


**Figure 1.** Reverse-vortex flow stabilization concept (a) and internal view of a reverse-vortex flow stabilized gliding arc (b).

Figure 1 (b) depicts the inner view of a reverse-vortex flow stabilized gliding arc reactor, in which the arc movement is demonstrated with a fast-shutter photograph. The bright cathode spot is very obvious, emitting strong black-body radiation. The cathode spot is a source of intense heat and thermionic emission, bringing the arc close to vibrational-translational equilibrium (i.e., the temperature of vibrationally excited molecules becomes equal to the gas kinetic temperature), in other words, there is no overpopulation of the vibrational levels compared to a thermal distribution. This hampers the energy efficiency for $CO_2$ conversion, as the $CO_2$ molecules dissociate thermally, rather than through the more efficient vibrational pathway [3,24].

The effect of heat insulation of the GA in a reverse-vortex flow has been shown through modelling [18,23]. With no doubt, the arc is indeed forced in the reactor centre [18,20]. This configuration, however, results in a quasi-static hot cathode spot on the cathode cap, as can be verified

by the photograph in figure 1 (b). Clearly, the GA manifests itself in different stages: the area closest to the cathode spot is mostly thermal, while closer to the anode the arc cools down. Some difference in light emission can be spotted in figure 1 (b), and variations in plasma density and temperature have been predicted through modelling [18,23]. Due to the intense arc contraction, the discharge is rather thin (see figure 1(b)), which was indeed verified in simulations [18] and experiments [20]. The discharge radius is typically no more than 2 mm. This means that only a limited portion of the gas actually passes through the plasma region and can be converted, while the rest leaves the reactor untreated, thus limiting the overall conversion. In addition, the maximum conversion capability of the reactor is limited by its ability to elongate the arc – whose maximum length is practically the distance between cathode and anode. The arc diminishes shortly after the anode, as is visible in figure 1(b).

## 3. Novel dual-vortex plasmatron (DVP): concept and design
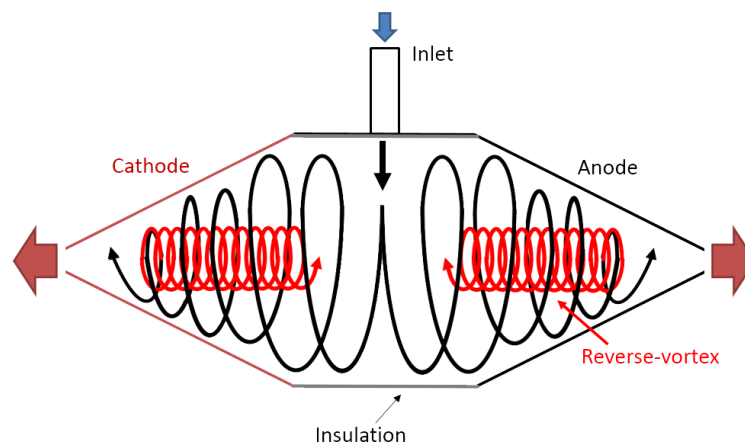


**Figure 2.** Concept of the novel dual vortex plasmatron (DVP). Here, the left electrode is designated as "cathode" by biasing it to a negative electric potential, with respect to the right electrode, which is grounded (hence "anode").

The new dual-vortex plasmatron (DVP) concept, presented for the first time in this work, is shown in figure 2. A single tangential inlet, creating a high flow velocity, is attached to an electrically insulating piece (Teflon®, ceramic or equivalent). Two hollow electrodes with conical shape are attached to the opposing sides, forming a symmetric vessel. The gas travels tangentially inside the reactor, forming two symmetric vortices. The two outlets have a small radius with respect to the main chamber radius, in order to facilitate high speed rotational flow at the outlet edge, causing rotation of the arc and cooling down of the cathode spot. The electrodes have a conical shape internally, which facilitates the formation of an inner, reverse vortex due to the rapidly decreasing radius of the main vortex. The hot cathode spot emerges at the negatively-biased electrode. The grounded electrode typically develops an "anode" spot, at much lower temperature.

The practical realisation was carried out with CNC machining at the University of Antwerp. The electrodes are made of stainless steel 316, and the insulation layer is made of Teflon®. The six bolts that hold the construction together are also non-conductive (figure 3). Non-conductive domains are depicted in blue in figure 3 (a). The produced reactor is 130 mm long when assembled. There is only one tangential inlet with ¼" NPT thread insert. The inlet internal diameter is 2 mm, to enable high gas flow velocity. The two outlets are terminated with ¼" NPT threads for steel tube insertion.
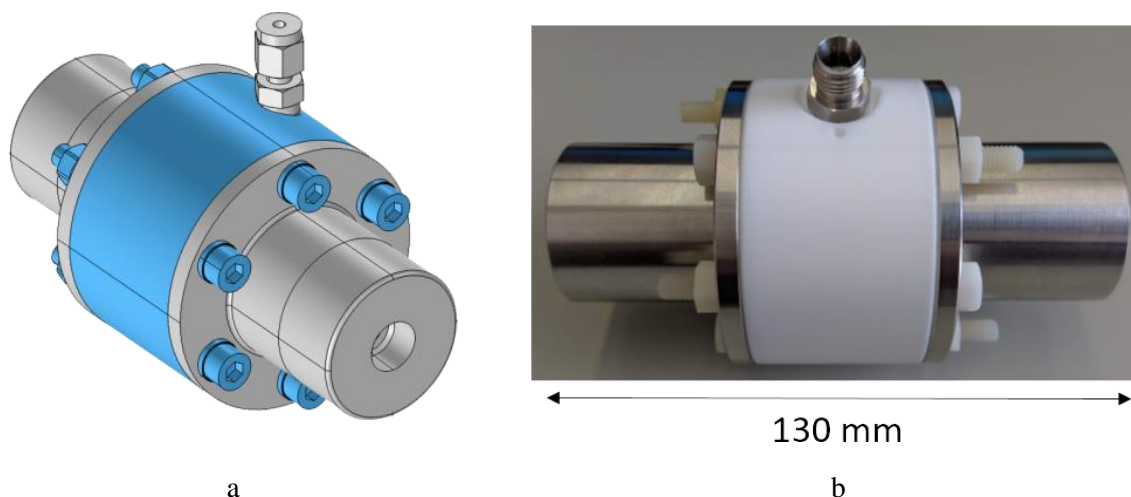
Figure 3. 3D CAD model of the DVP (a), and the machined unit (b).

The internal structure of the reactor can be viewed in detail in figure 4. A stepped insert in the Teflon® flange ensures correct placement and distancing for the electrodes. The arc ignition gap (start-up gap) is 2 mm long, and it also contains the single tangential inlet (see figure 4). The conical cavities in the electrodes are 44 mm long (each), with a large diameter of 24 mm and small diameter of 6.35 mm. The arc ignites at the start-up gap (shortest distance between the electrodes), but it is rapidly elongated by the fast tangential gas flow coming from the inlet. Gradually, it is extended sideways, in both directions towards both outlets, forming a long discharge of about 90 mm length (schematically illustrated in figure 4).
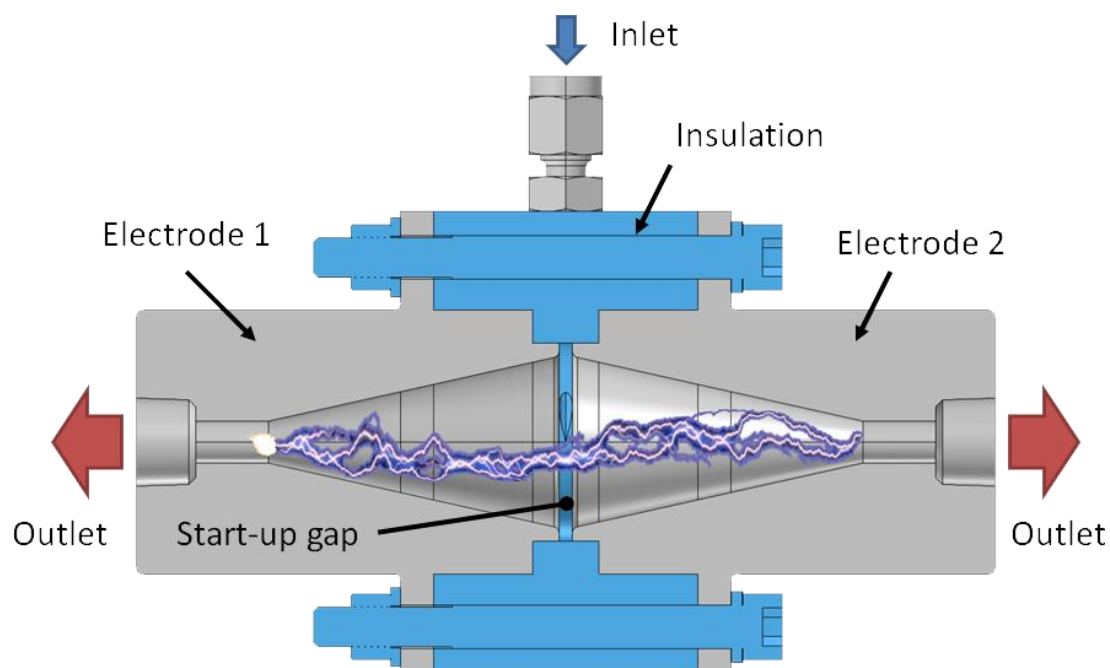


Figure 4. Half cut-off side view of the DVP, with artistic representation of the arc discharge (purple).

Electrodes 1 and 2 are completely identical, and neither is defined as cathode or anode – this only depends on the power supply polarity. The start-up voltage was predicted to be around 6 kV using Paschen curves, and is actually around 6.5 kV in the practical experiment. The electrode edges are filleted in order to prevent hot spot formation. Flow rates of 5 to 30 L/min are possible, the main limiting factors being the pressure on the tangential inlet and the cooling rate of the reactor.

## 4. Experimental setup
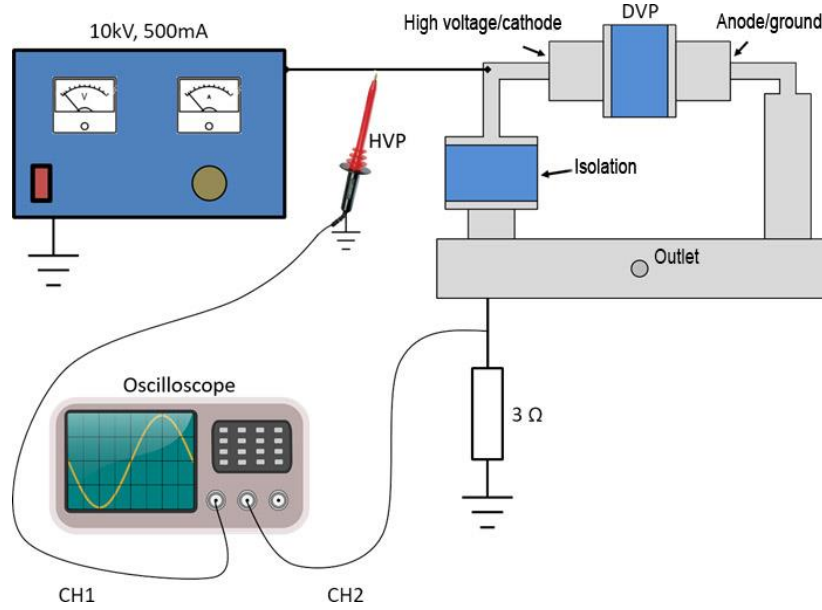


**Figure 5.** Electrical configuration of the experiment.

The electrical configuration of the experiment is shown in figure 5. A high voltage, switch-mode DC power supply, which can deliver 10 kV and 500 mA, is connected to the DVP. The DVP is mounted on a mixing console, which connects the two outlets into one, leading to the gas chromatograph (GC) for measuring the $CO_2$ concentration (see below). One side of this mixing console is isolated by an additional Teflon® piece (with a gap of 40 mm), as it is at high voltage. The voltage signal is measured with a high voltage probe (HVP) with a 1:1000 ratio. The current signal is acquired with a $3\Omega$ shunt resistor. A Keysight DSO-X 1102A 100MHz oscilloscope is used. The electrical power in the plasma is obtained from the product of voltage and current.

The gas composition is measured using an Interscience Compact GC, equipped with a thermal conductivity detector (TCD), and an Interscience Trace GC 1310, also utilizing a TCD detector, in order to assure systematic accuracy in the setup. Virtually no difference in the results was observed. A Bronkhorst El-Flow Select mass flow controller handles the gas input. The following formula is used to calculate the $CO_2$ conversion:

$$X_{GC,CO_2} = \frac{\dot{y}_{(in)} - \dot{y}_{(out)}}{\dot{y}_{(in)}} \tag{1}$$

where $\dot{y}_{(in)}$ is the $CO_2$ TCD peak area, measured in the GC without plasma, and $\dot{y}_{(out)}$ is the $CO_2$ peak area of the gas leaving the plasma reactor. The conversion value is corrected for the gas expansion using the following formula [25–27]:

$$X_{CO_2} = \frac{2X_{GC,CO_2}}{3 - X_{GC,CO_2}} \tag{2}$$

The specific energy input (SEI), which is an important parameter to determine the energy efficiency, is defined as:

$$SEI[kJ\ L^{-1}] = \frac{Plasma\ power\ [kW]}{Flow\ rate\ [\frac{L}{min}]} \times 60\ \frac{s}{min} \tag{3}$$

where the flow rate is defined as standard litres per minute (L/min) and the power (P) is the product of voltage (U) and current (I), i.e. P = U*I, as measured from the oscilloscope. The energy efficiency is defined as:

$$\eta[\%] = \frac{\Delta H_R[kJ\ mol^{-1}] \times X_{CO_2}[\%]}{SEI[kJ\ L^{-1}] \times 24.5\ L\ mol^{-1}} \tag{4}$$

where $\Delta H_R$ is the reaction enthalpy for $CO_2$ splitting at standard conditions (279.8 kJ mol$^{-1}$).

## 5. Electrical characterization of the DVP

Figure 6 illustrates the oscilloscope waveform taken from the DVP setup. The figure shows repetitive arc behavior (normal GA behavior), with some variation in the peak voltage/current values, which is again typical for a GA. The voltage peaks are slightly above 6 kV, which is the ignition point. The current peaks are up to 1 A. The period between the pulses is around 5 μs, which equals to 200 kHz repetition rate. Note that the signal might be influenced by the switching frequency of the power supply itself.

At the pulse edges, slight ripples are visible, possibly indicating an inductive load. This might be caused by the arc and the power supply cables combined. The average power from the obtained signal equals 460 W at 10 L/min, which is lower than for the reverse-vortex flow gliding arc plasmatron (GAP) system in [11], where values of 500-600W were reached.

The volt-amp characteristic (with time-averaged values) of the DVP is shown in figure 7. The minimum current to sustain the plasma was found to be 150 mA. Up to 200 mA, a slow increase of the voltage was observed. A sudden peak in the voltage appears at 240 mA, indicating a glow-to-arc transition [28]. While this is certainly an interesting phenomenon, the rather low accuracy of the power supply current regulation limits the number of data points that can be obtained for a more detailed study. The given setup demonstrates somewhat unstable behavior. The power supply is unable to supply enough current to sustain the arc above flow rates of 12.5 L/min. At 10 L/min, it is generally more stable, with reliable arc ignition and sustainment. At 15 L/min, the plasma could not be sustained long enough for reliable GC measurements. Lower flow rates (5 and 7.5 L/min were tested) do not provide enough cooling for the electrodes. This allows a limited working bracket for the gas flow rate.
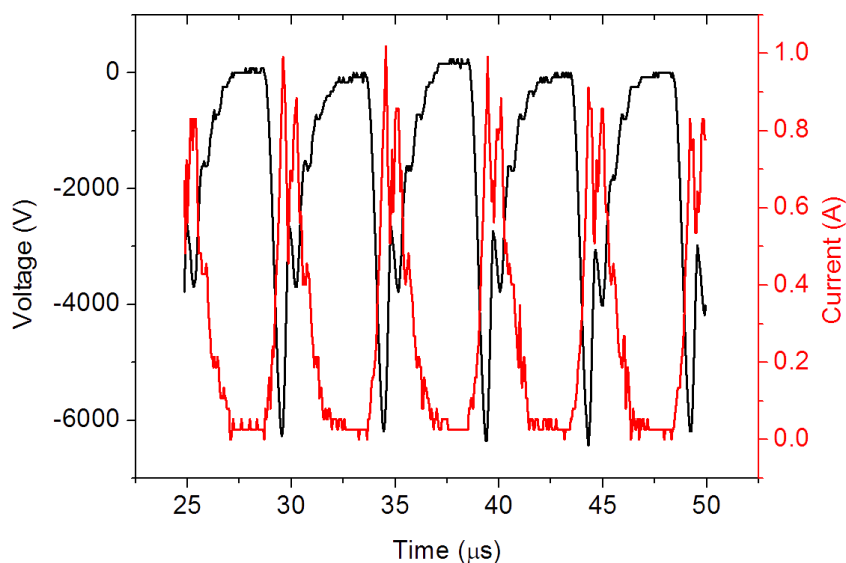


**Figure 6**. Oscilloscope waveform of the DVP, at 10 L/min, and 332 mA average current.
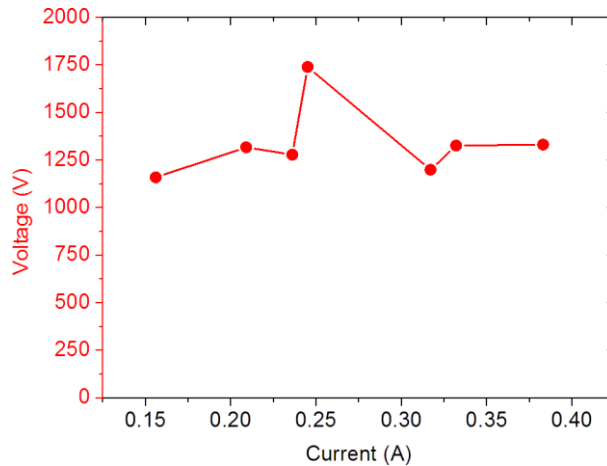
**Figure 7.** Volt-amp characteristic of the dual-vortex plasmatron, at 10 L/min.
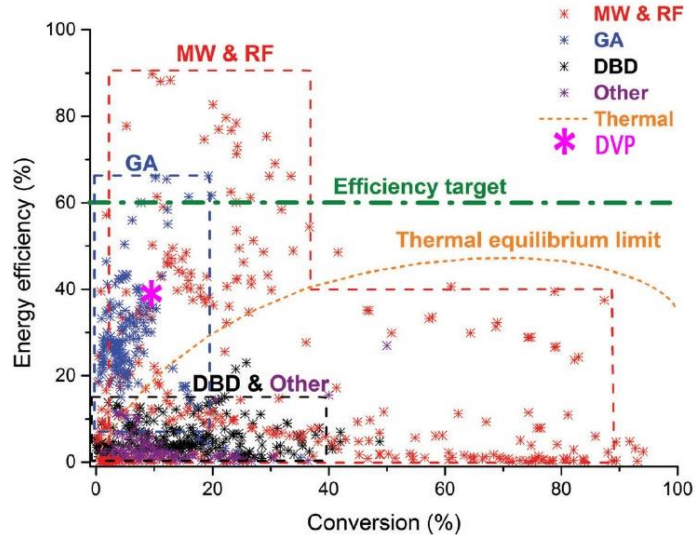
## 6. $CO_2$ conversion in the DVP

Figure 8 illustrates the $CO_2$ conversion (as calculated by eq. 1 and 2) and corresponding energy efficiency as a function of SEI, which is defined as the plasma power divided by gas flow rate (see eq. (3) above). Note that no stable discharge was obtained between 2.2 and 2.7 kJ/L. Lower SEI values than 1.95 kJ/L did not yield a sufficiently stable plasma either (for the GC measurements), as the arc would break up frequently due to low current. Values higher than 2.7 kJ/L did not provide sufficient cooling for the electrodes and the reactor body.

We could obtain a stable plasma at flow rates of 10 and 12.5 L/min. At 10 L/min and 446 W plasma power (i.e., the highest power possible in our experiments, yielding an SEI = 2.67 kJ/L), the highest $CO_2$ conversion of 9.5% is obtained, with the highest energy efficiency of 41%. This is higher than reported for other GA reactors (e.g., [10,11,15,29]). The conversion drops to 7.2% at 12.5 L/min for the same plasma power (SEI = 2.16 kJ/L), though a relatively high energy efficiency of 38% is still maintained. This lower conversion is attributed to the shorter residence time at higher flow rate. In addition, it suggests that the $CO_2$ conversion is mainly thermal. Indeed, the higher gas flow rate results in a somewhat lower gas temperature (see Figure 16 below), so that thermal conversion in the plasma is proportionally lower [3,9]. While the conversion increases almost linearly with increasing power, the energy efficiency tends to be consistently around 38%, which is very promising and advantageous compared to other plasma reactors (e.g., [7], [6,11,25], [30]), where the energy efficiency typically drops upon rising power. This also means that higher conversion rates should be attainable, and perhaps with the same high energy efficiency, using a different power supply with higher power capability. This will be the subject of our future work, after building a new power supply.
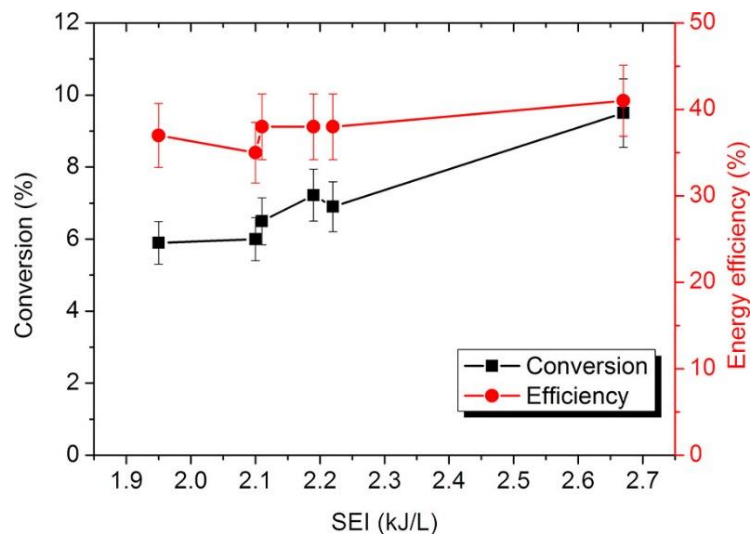


**Figure 8.** $CO_2$ conversion and energy efficiency for the DVP, as a function of SEI.

**Figure 9.** Performance of the DVP, in terms of energy efficiency and $CO_2$ conversion, in comparison with other plasma reactors; image adopted from [3].

In figure 9, we compare the energy efficiency and $CO_2$ conversion of the DVP to the performance of other plasma reactors for $CO_2$ conversion. While MW and RF discharges yield higher energy efficiency, these results were all obtained at reduced pressure, where more energy-efficient $CO_2$ conversion can be reached, due to a stronger overpopulation of the vibrational levels [3]. However, reduced pressure operation is less suitable for industry. Compared to other GA reactors, all operating at atmospheric pressure, we observe that some setups still yield better results, but some of these higher data points are based on model predictions for possible performance improvement (e.g., [14]), while others use dilution gases (e.g. [30]), which may enhance the absolute conversion (as plotted in figure 9), but reduces the effective, overall conversion (due to a lower fraction of $CO_2$ in the mixture). Generally, most data points are lower than in our DVP, both in terms of conversion and energy efficiency. The energy efficiency is also clearly above the results obtained in DBD reactors, and well above the thermal equilibrium limit (see orange curve).

The reader will observe that our results should better be compared to relevant systems only, however, for completeness and fairness, we do not want to omit any data from figure 9. For this reason, the DVP is placed in the global picture of plasma-based $CO_2$ splitting. However, the most "direct" comparison can be drawn with the RVF-based GA plasmatron presented in [26]. The clear-cut improvements of the DVP can be seen in the slightly higher (9.5%) conversion, and the high (up to 41%) energy efficiency thorough the entire operating range of the reactor. Furthermore, clearly less electrode degradation is observed, as the arc glides over a much larger surface. This is not reflected in figure 9, but is also an important point of consideration for practical use (i.e., improved reliability). Finally, we believe that our design is capable of utilizing higher power values due to its ability to elongate the discharge in two directions, therefore stabilizing a long arc with a high voltage drop, as explained in the introduction, but this will need to be tested in practice with a more powerful power supply.

In general, the present results are already quite promising. In the future, we want to further exploit the capabilities of the DVP, because also theoretically it is very promising, as illustrated by the modeling results below, but it is currently limited by the power supply available in our lab.

## 7. Fluid dynamics and plasma modelling

In order to characterize the gas flow behavior in the reactor, we developed a turbulent gas flow model within COMSOL Multiphysics [31]. The Navier-Stokes equations are solved for the mass and momentum conservation:

$$\nabla \cdot \boldsymbol{P} + f = \rho \frac{\partial \boldsymbol{u}}{\partial t} + \rho (\boldsymbol{u} \cdot \nabla) \boldsymbol{u} \qquad (5)$$

$$\frac{\partial \rho}{\partial t} + \nabla \cdot (\rho \boldsymbol{u}) = 0 \tag{6}$$

where $\boldsymbol{P}$ stands for the Cauchy stress tensor, $f$ represents the fluid body force, $\rho$ stands for fluid density and $\boldsymbol{u}$ is the gas flow vector. The turbulence description follows the so-called k-epsilon model (see [23]).

Next to describing the gas flow pattern, we also developed a plasma model, based on the drift-diffusion quasi-neutral fluid model, as explained in detail in [32]. Although the DVP is developed for $CO_2$ conversion (and other gas conversion applications), a 3D plasma model in $CO_2$, including all chemistry (i.e., various types of ions, radicals, vibrationally and electronically excited levels), would yield excessive calculation times. Therefore, we developed a 3D model for argon, with limited chemical reaction set, as in [23]. We only considered the Ar ground state atoms, Ar excited atoms in the 4s levels (i.e., four lowest excitation levels), the $Ar^+$ ions and the electrons, and only four reactions, listed in Table 1. This limited reaction set is optimized for 3D computations, and bears reasonable accuracy compared to more complete reaction sets [23]. Note that $Ar_2^+$ ions might also be important at atmospheric pressure, but in our previous model for an APGD [9], operating at similar conditions, and also atmospheric pressure, we included these ions (with Argon set), but they did not significantly affect the calculation results. Because adding these ions results in a higher computational cost, we did not include them in the present model.

**Table 1. Reaction set for the 3D Ar model**

| | Reaction | Rate coefficient (k) | Ref. |
|---|---|---|---|
| **1.** | e + Ar → e + Ar | BS | [33] |
| **2.** | e + Ar → e + Ar(4s) | BS | [33] |
| **3.** | e + Ar(4s) → 2e + Ar$^+$ | BS | [33] |
| **4.** | Ar$^+$ + e + Ar → Ar + Ar | $1.5 \times 10^{-40} \left(\frac{T_g}{300}\right)^{-2.5}$ | [34] |

BS = Boltzmann solver [35]. It means that the rate coefficients are obtained from the corresponding energy-dependent cross sections and an electron Boltzmann equation, which calculates the electron energy distribution function for fixed electric field values.

The following balance equation is solved for the $Ar^+$ ion density:

$$\frac{\partial n_i}{\partial t} + \nabla . \left(-D_i \nabla n_i + \mu_i n_i \overrightarrow{E_{amb}}\right) + (\boldsymbol{u}. \nabla)n_i = R_i \tag{7}$$

where $n_i$ stands for the ion density, $\mu_i$ for ion mobility coefficient, $D_i$ for ion diffusion coefficient, $\vec{E}_{amb}$, for the ambipolar electric field (see below), $\boldsymbol{u}$ for the gas velocity vector, and $R_i$ is the ion production term.

For the Ar excited atom density, the following equation is solved:

$$\frac{\partial n_*}{\partial t} + \nabla \cdot \left(D_* \vec{\nabla} n_*\right) + \left(\overrightarrow{u_g} \cdot \vec{\nabla}\right)n_* = R_* \tag{8}$$

where $n_*$ stands for the species density, $D_*$ for the diffusion coefficient, $\boldsymbol{u}$ for the gas velocity vector, and $R_*$ is the species production term.

As the model is quasi-neutral, the density of $Ar^+$ ions and electrons is assumed to be equal. Hence, the electron balance equation does not have to be solved. The ambipolar electric field $\overrightarrow{E_a}$ is obtained from:

$$\overrightarrow{E_a} = \frac{(D_i - D_e)\nabla n_{pl}}{(\mu_i + \mu_e)n_{pl}} \tag{9}$$

where $n_{pl}$ is the density of the plasma.

The following equation is solved for the electron energy balance, to obtain the average electron energy:

$$\frac{\partial n_e \bar{\varepsilon}_e}{\partial t} + \nabla \cdot \left(D_{\varepsilon,e}\vec{\nabla}(n_e\bar{\varepsilon}_e) - \mu_{\varepsilon,e}n_e\bar{\varepsilon}_e\vec{E}\right) + \left(\vec{u_g} \cdot \vec{\nabla}\right)n_e\bar{\varepsilon}_e = |q_e|\vec{E} \cdot \vec{G_e} + n_e\Delta\bar{\varepsilon}_e + Q_{bg} \tag{10}$$

where $D_{\varepsilon,e}$ stands for the electron energy diffusion coefficient, $\mu_{\varepsilon,e}$ is the electron energy mobility, and $\vec{E} = \vec{E}_a$, (see above). In the equation, $|q_e|\vec{E} \cdot \vec{G_e}$ is the electromagnetic heating term, $n_e\Delta\bar{\varepsilon}_e$ accounts for the averaged electron elastic and inelastic energy losses upon collisions, and $Q_{bg}$ stands for additional background heating, a common modelling approach to reduce the slope of the gradient [23,36].

In addition, the gas temperature is obtained by solving the heat balance equation, which incorporates the turbulent heat conductivity, calculated using the Kays-Crawford model [37]:

$$\rho C_p \frac{\partial T_g}{\partial t} + \rho C_p \boldsymbol{u} \cdot \nabla T_g - \nabla \cdot \left((k_g + k_T)\nabla T_g\right) = Q \tag{11}$$

where $\rho$ is the gas density, $C_p$ is the heat capacity of the gas, $k_g$ is the thermal conductivity and $k_T$ is the turbulent thermal conductivity of the gas, $T_g$ is the gas temperature, $\boldsymbol{u}$ is the gas velocity vector and $Q$ accounts for the source of gas heating. The sum of the gas ($k_g$) and turbulent ($k_t$) heat conductivity results in the effective heat conductivity $k_{eff}$.

Finally, the current conservation equation reads:

$$\vec{\nabla} \cdot \left[-\sigma\vec{\nabla}\varphi - |q_e|\left(D_i\vec{\nabla}n_i + D_e\vec{\nabla}n_e\right)\right] = 0 \tag{12}$$

where $\sigma$ stands for the plasma conductivity, $\varphi$ stands for the electric potential, $|q_e|$ is the elementary charge, and $D_e$ and $n_e$ stand for the electron diffusion coefficient and density, respectively.
The boundary conditions for the plasma model are shown in table 2.

**Table 2. Boundary conditions for the 3D Ar model**

| Boundary | Expression | Note | Equation |
|---|---|---|---|
| Walls | $-\vec{n} \cdot \left(-D_i\nabla n_i - \mu_i n_i\overrightarrow{E_{amb}}\right) = 0$ | No flux | Ion density balance |
| Walls | $-\vec{n} \cdot \left(-\mu_{\varepsilon,e}n_e\overrightarrow{E_{amb}} - D_{\varepsilon,e}\nabla(n_e\bar{\varepsilon}_e)\right) = 0$ | No flux | Electron energy balance |
| Walls | $-\vec{n} \cdot (D_*\nabla n_*) = 0$ | No flux | Excited species balance |
| Walls | $-\vec{n} \cdot \left(-k\nabla T_g\right) = 0$ | Adiabatic walls | Heat balance |
| Cathode | 2000V | Voltage | Current conservation |
| Anode | 0V | Ground | Current conservation |

## 8. Calculated flow velocity profiles

Figure 10 illustrates the gas flow velocity profile for a flow rate of 10 L/min. The streamlines represent the velocity vector, while the colour indicates the total velocity magnitude.
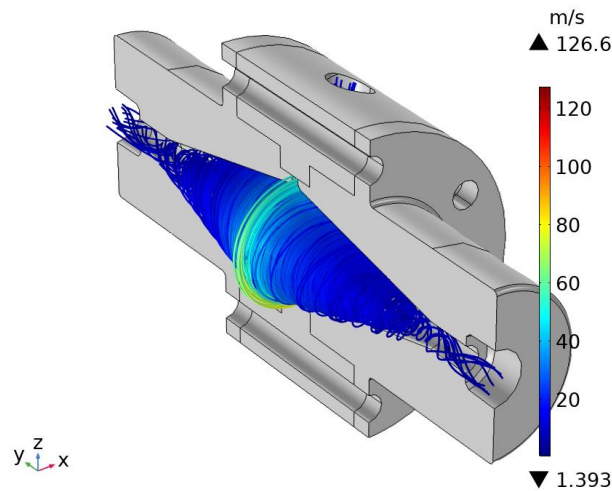


**Figure 10.** Calculated gas flow velocity streamlines at a flow rate of 10 L/min (m/s). Half-cut 3D view.

The velocity at the start-up gap is above 100 m/s, and follows a rotational motion that is preserved towards the outlets of the reactor. The velocity magnitude in the main parts of the reactor is in the order of 10-40 m/s. The vortex development is symmetric in both directions. Figure 11 shows a detail of the flow profile near one of the outlets. Normally, a cathode (or anode) spot attachment would occur in this region, on the outlet edge. In the present design, however, the high rotational velocity of the flow allows the cathode (or anode) spot to rotate along the outlet edge, which reduces the heating and hence the damage of the electrode.
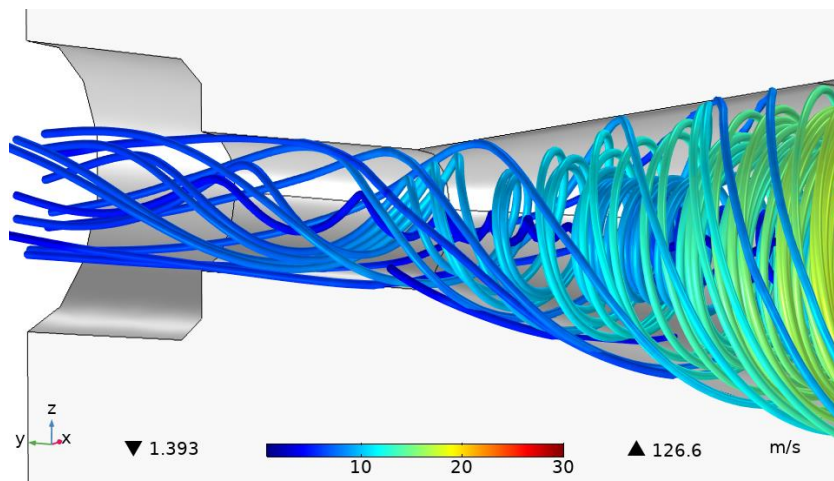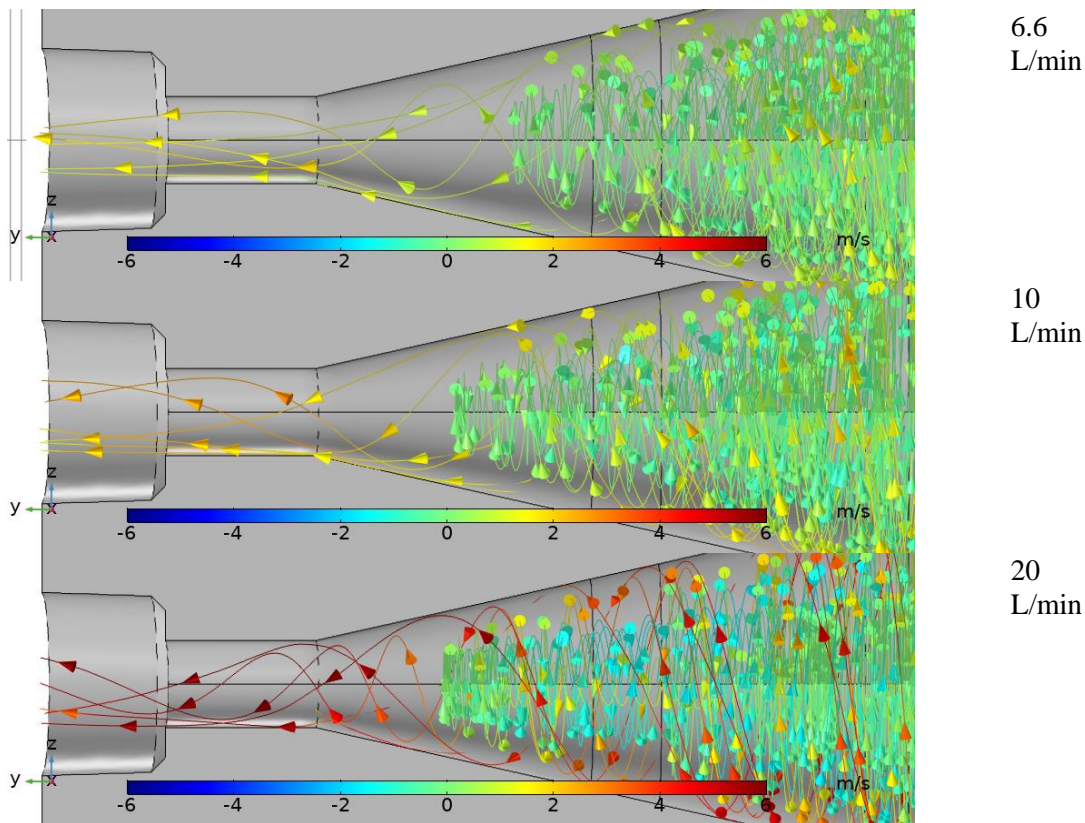


**Figure 11.** Detail of the calculated gas flow velocity streamlines at one of the electrode ends. Flow rate: 10 L/min.

In figure 12, we plot the detailed gas flow profiles with arrow lines in one part of the reactor, for three different flow rates, i.e., 6.6, 10 and 20 L/min. The colour now indicates the magnitude of the axial velocity component (i.e., on the y-axis). Although our power supply does not allow yet to reach a stable plasma above flow rates of 12.5 L/min (cf. section 6 above), we believe these higher flow rates could be beneficial for arc cooling, and thus to reach more energy-efficient $CO_2$ conversion, as well as limited electrode damage.

Hence, we want to investigate their effect computationally, where we are not bound by power supply limitations. Indeed, if the model predicts promising results, it could guide our experiments to further improvements.

The flow is essentially separated into forward flowing (positive values, i.e. green to red) and backward flowing (negative values, i.e. green to blue). We can distinguish the presence of a secondary reverse-vortex in the gas flow for all three cases. At low flow rate (6.6 L/min), this reverse vortex is quite weak, with backward velocity of around 1 m/s. At 10 L/min, the reverse vortex travels backwards at about 2 m/s. At the highest flow rate of 20 L/min, the reverse vortex is very pronounced, with backward velocity of up to 4 m/s. The surrounding forward vortex (with forward velocity) travels much faster, i.e., at 2-3 m/s for 6.6 and 10 L/min, and up to 6 m/s at 20 L/min. This means that in addition to the rotational flow behaviour near the outlets, which reduces electrode heating and damage, the DVP also exhibits reverse-vortex flow behaviour to some extent. The reverse-vortex flow has been discussed before as a very effective method for plasma stabilization and insulation [1,23], as demonstrated both by experiments [10,11] and modelling [23]. Generally, the reverse-vortex flow contributes well to efficiently sustaining the plasma by insulating it from the reactor walls and thus preventing heat losses. It also improves the gas mixing, and lowers the gas temperature through intense turbulent heat transport [18].



**Figure 12.** Calculated gas flow velocity streamlines near one of the electrode ends, at three different flow rates. The colour indicates the axial flow velocity (along the y-axis).

## 9. Calculated plasma behaviour

The plasma modelling was carried out in two stages – for initial discharge conditions at arc ignition, and when the plasma reaches a quasi-stationary state. We already showed in [23] that the arc glides into a quasi-stationary "stabilized" state with little axial rotation after a certain amount of time, which depends on the reactor design and gas flow rate. In [23] this state was achieved after 1 ms for a conceptual reverse-vortex flow GA reactor geometry, while in [18], a stationary state was achieved after 5 ms for the actual reverse-vortex flow GAP reactor geometry. Generally, as the model does not include complex features, such as arc re-ignition and cathode (or anode) spot attachments, the gliding process is smooth

with relatively small changes in the plasma parameters. For this reason, we present here only the initial and final (steady-state) stage of the arc, to preserve a reasonable computation time. The streamer stage of the arc is mimicked by a short time-dependent artificial heating function.
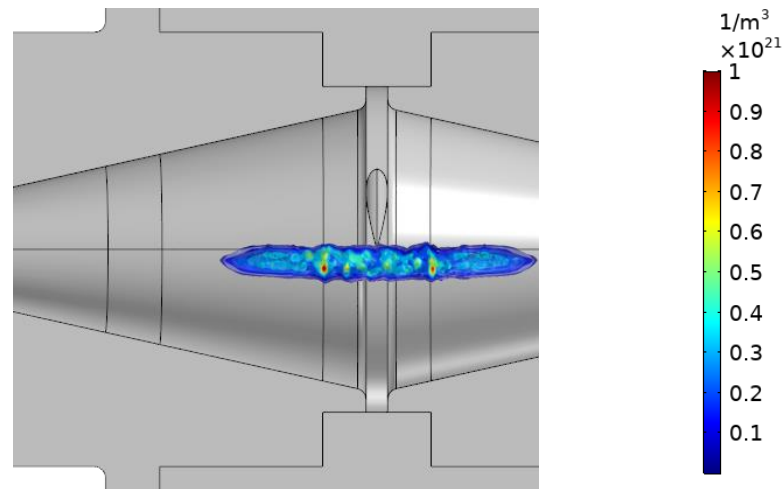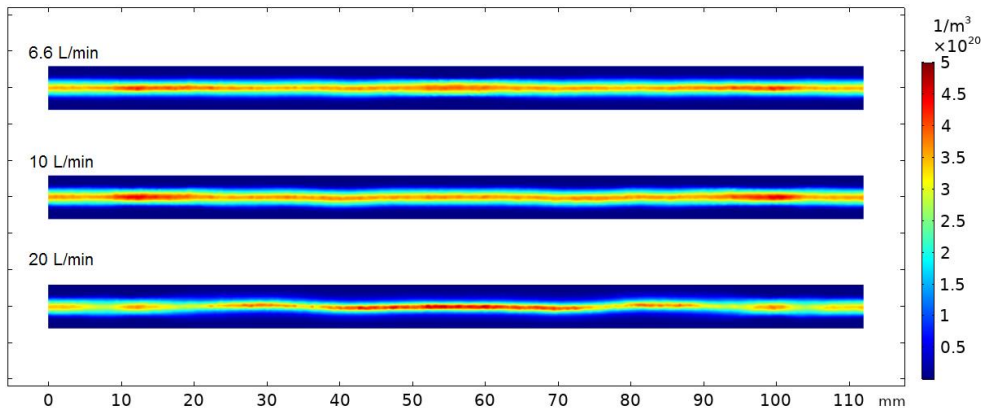


**Figure 13.** Calculated plasma density for the initial arc stage at 11 µs, at 460 mA arc current and 10 L/min gas flow rate.

Figure 13 depicts the arc development just in front of the tangential inlet inside the reactor. This is the initial stage of the plasma, indicating a short, straight column, gliding at the shortest distance between the two electrodes (see figure 4). For this computation, the full internal body of the reactor was modelled, with 490,000 mesh elements. This severely prohibits longer computation times, which would be needed for further arc extension. However, the arc electrode attachment and gliding can be observed from the calculations. The calculated plasma density is in the range of $1$-$8 \times 10^{20}$ m$^{-3}$, which is typical for a GA in argon [12,23,38]. The discharge fills around 8% of the total reactor volume.
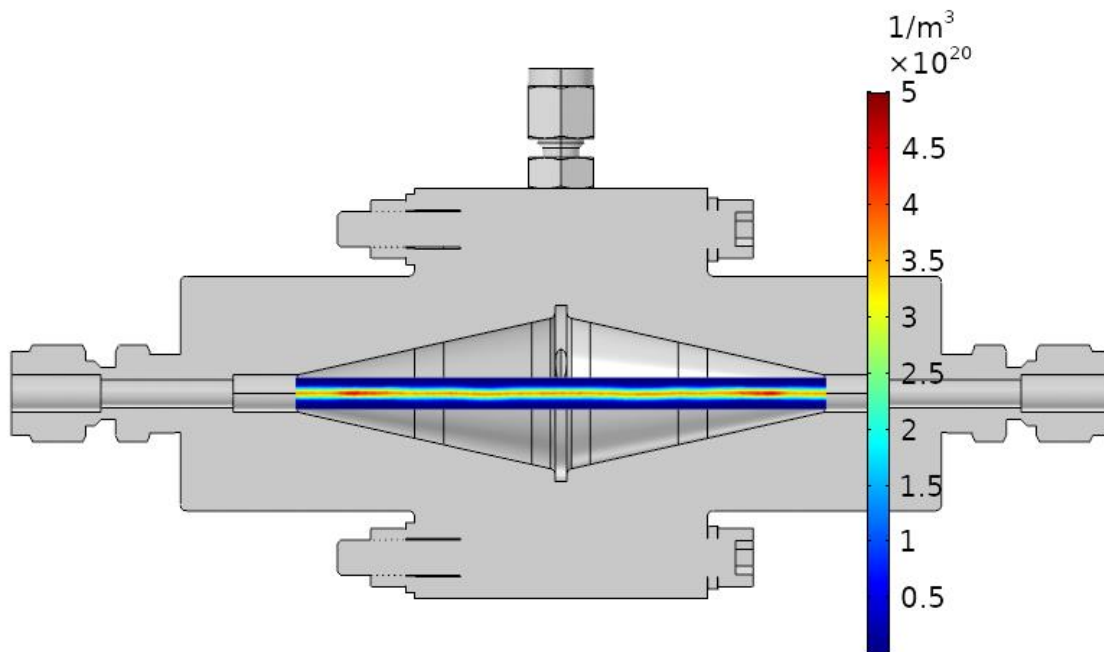


**Figure 14.** Calculated plasma density in the fully elongated arc at steady-state (1 ms), at 460 mA arc current and 10 L/min gas flow rate.

**Figure 15.** Calculated plasma density in the fully elongated arc at steady-state (1 ms), for three different gas flow rates, at 460 mA.

Figures 14 and 15 illustrate the fully elongated state of the arc, i.e. stabilized in the reactor centre, in the entire reactor design (figure 14) and a detailed view for three different gas flow rates (figure 15). At the highest flow rate (20 L/min), the arc demonstrates some bending, as a result of the spiral-like flow profile. Furthermore, the plasma density in the centre is slightly higher (around $5 \times 10^{20}$ m$^{-3}$) than at the low flow rate of 6.6 L/min, due to the stronger convection coefficient. The spiral pattern of the arc at 20 L/min will be able to cover a larger portion of the reactor volume, thus enabling a larger fraction of the gas to be treated by the arc, which will improve the conversion.
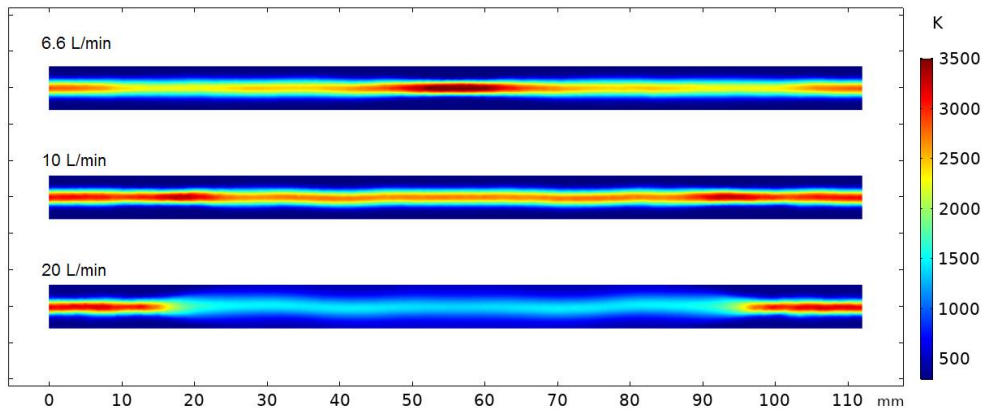


**Figure 16.** Calculated plasma gas temperature at steady-state (1 ms), for three different gas flow rates, at 460 mA.

Figure 16 depicts the calculated gas temperature. At 6.6 L/min, the gas temperature reaches 3500 K in the centre of the arc, cooling down to about 2000 K towards the sides, but rising again to 3000 K near the electrodes. At 10 L/min, the temperature is more homogeneous along the arc length, with values around 2800-3000 K, and slightly lower in the center. A striking difference can be observed at the high flow rate of 20 L/min. A large portion of the arc (between 20 and 90 mm; see the scale at the bottom) is rapidly cooled to 1500 K and below. This effect is attributed to turbulent heat transfer [18,37], and the development of a reverse-vortex flow (figure 12) leads to additional heat transfer. The calculated temperatures are comparable to earlier studies for a classical GA [12,36]. The lower gas temperature is highly beneficial for a vibrational-translational non-equilibrium, and thus for more energy-efficient $CO_2$ conversion. Hence, the high flow rate of 20 L/min looks very promising in this regard, both with respect to the larger portion of the reactor volume covered by the arc (figure 15) and the lower gas temperature, allowing more vibrational-translational non-equilibrium. This is further confirmed in figure 17, where the discharge temperature and effective (material + turbulent) thermal conductivity (see section 7) are averaged over a line at the discharge centre. The figure clearly shows that the threshold for turbulent heat transfer intensification is around 10 L/min. In the range of 10-20 L/min, the turbulent conductivity rapidly enhances the effective heat conductivity from ~0.2 to 1.6 W/(m*K), which directly results in a lower gas temperature.
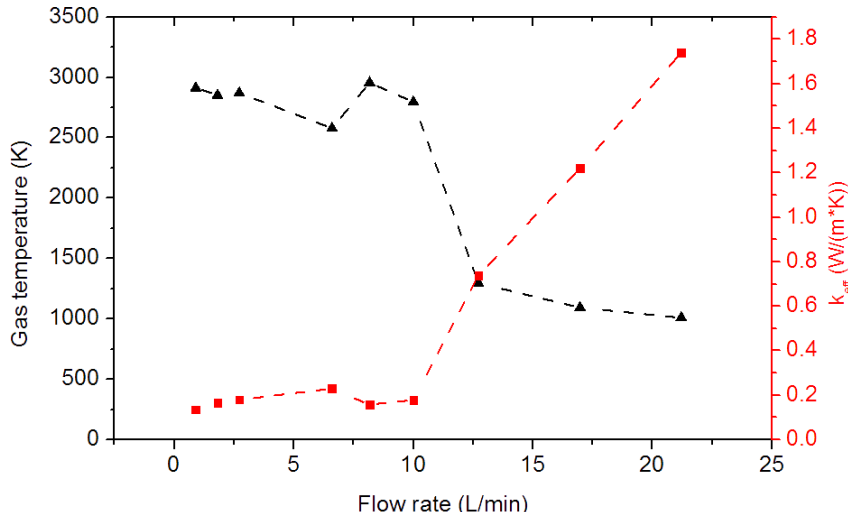
**Figure 17.** Gas temperature and effective thermal conductivity as a function of flow rate.

Our next step in this research will be to design a new power supply that can handle higher flow rates, in order to evaluate these conditions experimentally, and to verify whether they indeed result in enhanced and more energy-efficient $CO_2$ conversion.

In figure 18, we clarify the reason for the significantly lower temperature at the highest gas flow rate. It is attributed to turbulent heat transfer, which has its maximum intensity at the areas of low gas temperature, indicated in figure 16. Interestingly, the turbulent heat transfer seems completely different for different gas flow rates. At a flow rate of 6.6 L/min, two heat exchange zones can be observed at 10-30 and 80-100 mm (see length scale in figure 18), while the turbulent heat exchange in the centre is very low, as confirmed by the maximum temperature in figure 17. At 10 L/min, the turbulent heat exchange zones spread from the discharge centre, but with a rather low magnitude (around $2x10^5$ W/m²), which explains the homogeneous temperature distribution for 10 L/min, shown in figure 16. At 20 L/min, the highly turbulent zones are clearly visible (see figure 17), which explains the pronounced drop in temperature in the center (cf. figure 16).
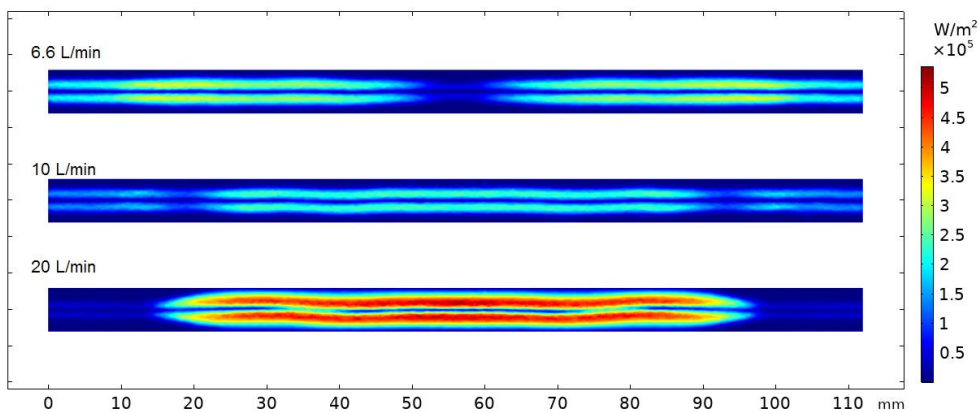


**Figure 18.** Calculated turbulent heat flux magnitude around the plasma, for three different gas flow rates, at 460 mA.

A constant electron temperature of about 2.5 eV is predicted for the three different gas flow rates, as is evident from figure 19. This is similar to [23], where the electron temperature was also rather independent of the gas temperature and flow rate. At 20 L/min, the electron temperature exhibits a broader profile in the radial direction, which can be explained by the lower arc contraction at lower gas temperatures, and by the spiral movement of the arc (cf. figure 15). We expect that this will again be more beneficial for the $CO_2$ conversion, because it will give rise to more electron impact vibrational excitation and direct electron impact dissociation of $CO_2$. Again, this will have to be evaluated experimentally in our future work.
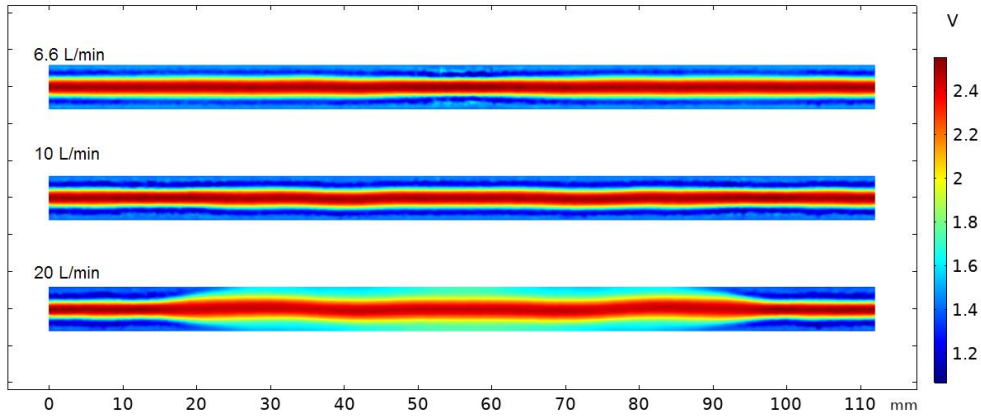
**Figure 19.** Calculated electron temperature at steady-state, for three different gas flow rates, at 460 mA.

In general, lower gas temperatures would be preferable, as they enhance the vibrational-translational non-equilibrium in the plasma, and promote the more efficient vibrational-induced $CO_2$ dissociation [3]. In the case of the reverse-vortex flow GAP [10,11], a gas temperature of 3000 K was calculated for $CO_2$ plasma (see [18]), and 5500 K was measured experimentally with $N_2$ [19]. These values are too high for (energy-efficient) vibrational-induced $CO_2$ conversion [1], [3], but they point towards mainly thermal conversion. The demonstrated turbulent cooling capability of the DVP, at least at high gas flow rates of 20 L/min, indicates the potential for high energy efficiency and high power handling, which can improve the overall conversion, if also the fraction of gas passing through the arc is enhanced. Following the calculations in [18], the gas temperature will be much higher in $CO_2$ than in argon. It is not possible to predict how much higher will be the gas temperature, as it depends on many variables, but in [18], the temperature was almost three times higher in $CO_2$ than in argon, i.e., around 3000 K vs 1000-1300 K. Therefore, a higher temperature is also expected for the DVP operating in $CO_2$, which again points towards higher flow rates in order to be able to achieve vibrational-translational non-equilibrium.
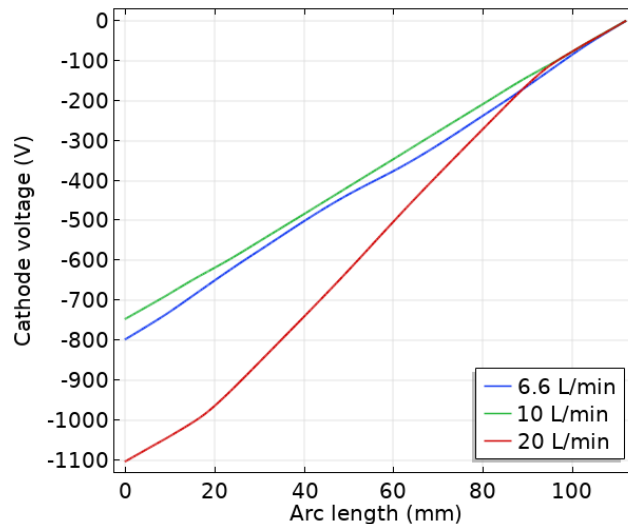


**Figure 20.** Calculated cathode voltage drop for three different gas flow rates, at 460 mA.

Figure 20 illustrates the calculated voltage drop across the discharge centre. The two lower flow rates yield a similar voltage drop of around 750-800 V. At 20 L/min, the voltage drop increases significantly to around 1100 V, indicating a lower plasma conductivity. Indeed, the volume-averaged plasma conductivity in the case of 6.6 and 10 L/min is 7.22 and 7.91 S/m, respectively, while in the case of 20 L/min, it is 4.78 S/m. This is to be expected from the intensive arc cooling, leading to a lower gas temperature and a drop in plasma density in certain arc areas (see figures 14 and 15). This result might

be interesting for experiments, as it indicates that a sudden increase in turbulent heat flux (beneficial for arc cooling, and thus to reach an energy-efficient regime for $CO_2$ conversion) can be detected through measuring the voltage drop across the plasma.

## 7. Conclusion

In this work, we designed a completely new GA plasma reactor concept from scratch, to be used for $CO_2$ conversion, based on insights obtained from computer simulations, i.e., a dual-vortex (GA) plasmatron (DVP) reactor. We extensively investigated this DVP reactor using fluid flow, heat transfer and plasma modeling. The calculated plasma characteristics, such as plasma gas temperature, electron density and temperature, are comparable to results in literature for other GA plasmas.

This novel reactor concept yields strong rotational gas flow, up to the electrode outlets, as demonstrated from the gas fluid dynamics simulations. This allows rotating the cathode (or anode) hot spots, and thus reduces electrode damage. Electrode degradation needs to be checked on the long-term, but currently, no observable pitting in the reactor electrodes was present for 10 experiments of 30 min each, which is a very good sign for the reactor reliability.

The results obtained with this DVP, in terms of $CO_2$ conversion and energy efficiency are currently limited by the power supply, to yield a stable plasma at gas flow rates above 12.5 L/min. Nevertheless, they are very encouraging: a good energy efficiency (up to 41%) is obtained at a $CO_2$ conversion around 9%, for a flow rate of 10 L/min. These values are comparable or better than other GA results in literature (e.g., [3,10,11,15]). However, they point towards mainly thermal conversion in the plasma, which is also the case in other GA and MW plasmas at atmospheric pressure (e.g., [5,10,39,40]. This is indeed confirmed by our modeling results, which indicate a high gas temperature around 3000 K, at a gas flow rate of 10 L/min, even in argon. Our model calculations, however, also predict that at higher flow rate of 20 L/min, the gas temperature would be significantly lower, due to strong turbulent heat transfer. This would enhance the vibrational-translational non-equilibrium in the plasma, and thus promote vibrational-induced dissociation of $CO_2$ molecules, which is the most energy-efficient pathway for $CO_2$ conversion [1,3]. Nevertheless, these calculations were for argon, while in $CO_2$ the gas temperature will be higher [18], again pointing towards using higher gas flow rates as being promising for more energy-efficient $CO_2$ conversion.

Using an Ar plasma model to describe a $CO_2$-operating plasma reactor is of course an approximation. However, the essentially three-dimensional nature of the problem leaves little choice due to computational limitations; in addition, the model results intend to show the tendency of decreasing temperature as a function of the internal flow turbulence.

Currently, the main obstacle towards using the full potential of the reactor is the power supply unit. As the rotating plasma is a highly reactive load, the strain on the power supply caused by reflected power is very high, and higher flow rates resulted in plasma instabilities. We plan to build such a power supply in the future, to allow stable plasma operation at higher flow rates, and thus, to further enhance the performance of the DVP. In addition, further developments might also include a de Laval nozzle [41] for rapid flow quenching at the outlets, in order to further enhance the $CO_2$ conversion by avoiding the backward reaction to occur.

Further research will thus include studying the electrical behavior of the GA, and the relation between the power supply system and the plasma stability. Finally, the DVP is also an interesting case for studying glow-to-arc transition and flow turbulence in a plasma.

## References

[1]    A. Fridman, Plasma chemistry, 1st ed., Cambridge University Press, New York, 2008.

https://doi.org/10.1017/CBO9780511546075.

[2]     A. Bogaerts, A. Berthelot, S. Heijkers, S. Kolev, R. Snoeckx, S. Sun, G. Trenchev, K. Van Laer, W. Wang, CO 2 conversion by plasma technology: Insights from modeling the plasma chemistry and plasma reactor design, Plasma Sources Sci. Technol. (2017). https://doi.org/10.1088/1361-6595/aa6ada.

[3]     R. Snoeckx, A. Bogaerts, Plasma technology-a novel solution for CO2 conversion?, Chem. Soc. Rev. 46 (2017) 5805–5863. https://doi.org/10.1039/c6cs00066e.

[4]     T. Kozák, A. Bogaerts, Evaluation of the energy efficiency of CO2 conversion in microwave discharges using a reaction kinetics model, Plasma Sources Sci. Technol. 24 (2015) 015024. https://doi.org/10.1088/0963-0252/24/1/015024.

[5]     W. Bongers, H. Bouwmeester, B. Wolf, F. Peeters, S. Welzel, D. van den Bekerom, N. den Harder, A. Goede, M. Graswinckel, P.W. Groen, J. Kopecki, M. Leins, G. van Rooij, A. Schulz, M. Walker, R. van de Sanden, Plasma-driven dissociation of CO2 for fuel synthesis, Plasma Process. Polym. 14 (2017) 126. https://doi.org/10.1002/ppap.201600126.

[6]     D.C.M. van den Bekerom, J.M.P. Linares, T. Verreycken, E.M. van Veldhuizen, S. Nijdam, G. Berden, W.A. Bongers, M.C.M. van de Sanden, G.J. van Rooij,  The importance of thermal dissociation in CO 2 microwave discharges investigated by power pulsing and rotational Raman scattering , Plasma Sources Sci. Technol. (2019). https://doi.org/10.1088/1361-6595/aaf519.

[7]     R. Snoeckx, R. Aerts, X. Tu, A. Bogaerts, Plasma-based dry reforming: A computational study ranging from the nanoseconds to seconds time scale, J. Phys. Chem. C. 117 (2013) 4957–4970. https://doi.org/10.1021/jp311912b.

[8]     R. Aerts, W. Somers, A. Bogaerts, Carbon Dioxide Splitting in a Dielectric Barrier Discharge Plasma: A Combined Experimental and Computational Study, ChemSusChem. (2015). https://doi.org/10.1002/cssc.201402818.

[9]     G. Trenchev, A. Nikiforov, W. Wang, S. Kolev, A. Bogaerts, Atmospheric pressure glow discharge for CO 2 conversion: Model-based exploration of the optimum reactor configuration, Chem. Eng. J. 362 (2019) 830–841. https://doi.org/10.1016/j.cej.2019.01.091.

[10]    T. Nunnally, K. Gutsol, A. Rabinovich, A. Fridman, A. Gutsol, A. Kemoun, Dissociation of CO2 in a low current gliding arc plasmatron, J. Phys. D. Appl. Phys. 44 (2011) 274009. https://doi.org/10.1088/0022-3727/44/27/274009.

[11]    M. Ramakers, G. Trenchev, S. Heijkers, W. Wang, A. Bogaerts, Gliding Arc Plasmatron: Providing an Alternative Method for Carbon Dioxide Conversion, ChemSusChem. 10 (2017). https://doi.org/10.1002/cssc.201700589.

[12]    A. Czernichowski, Spectral and electrical diagnostics of gliding arc, Acta Phys. Pol. A. 89 (1996) 595–603. https://doi.org/10.12693/APhysPolA.89.595.

[13]    G. Elaragi, Discharge Characteristics of Gliding Arc Plasma Reactor With Argon/Nitrogen, J. Adv. Phys. 7 (2015) 1316–1323. https://doi.org/10.24297/jap.v7i1.1736.

[14]    S.R. Sun, H.X. Wang, D.H. Mei, X. Tu, A. Bogaerts, CO2 conversion in a gliding arc plasma: Performance improvement based on chemical reaction modeling, J. CO2 Util. 17 (2017) 220–234. https://doi.org/10.1016/j.jcou.2016.12.009.

[15]    A. Indarto, D.R. Yang, J.-W. Choi, H. Lee, H.K. Song, Gliding arc plasma processing of CO2 conversion., J. Hazard. Mater. (2007). https://doi.org/10.1016/j.jhazmat.2006.12.023.

[16]    S.C. Kim, Y.N. Chun, Development of a gliding arc plasma reactor for CO 2 destruction, Environ. Technol. (United Kingdom). (2014). https://doi.org/10.1080/09593330.2014.925979.

[17]    X. Tu, J. Gallon, J. Whitehead, Electrical and optical diagnostics of atmospheric pressure argon gliding arc, in: Belfast (Ed.), 30th ICPIG (Belfast), 2011.

[18]    G. Trenchev, S. Kolev, W. Wang, M. Ramakers, A. Bogaerts, CO 2 conversion in a gliding Arc plasmatron: Multidimensional modeling for improved efficiency, J. Phys. Chem. C. 121 (2017) 24470. https://doi.org/10.1021/acs.jpcc.7b08511.

[19]    S. Gröger, M. Ramakers, M. Hamme, J.A. Medrano, N. Bibinov, F. Gallucci, A. Bogaerts, P. Awakowicz, Characterization of a nitrogen gliding arc plasmatron using optical emission spectroscopy and high-speed camera, J. Phys. D. Appl. Phys. 52 (2019) 1361. https://doi.org/10.1088/1361-6463/aaefe4.

[20]    M. Ramakers, J.A. Medrano, G. Trenchev, F. Gallucci, A. Bogaerts, Revealing the arc

dynamics in a gliding arc plasmatron: A better insight to improve $CO_2$ conversion, Plasma Sources Sci. Technol. 26 (2017). https://doi.org/10.1088/1361-6595/aa9531.

[21] A. Gutsol, J.A. Bakken, A new vortex method of plasma insulation and explanation of the Ranque effect, J. Phys. D. Appl. Phys. 31 (1998) 704–711. https://doi.org/10.1088/0022-3727/31/6/018.

[22] C.S. Kalra, Y.I. Cho, A. Gutsol, A. Fridman, T.S. Rufael, Gliding arc in tornado using a reverse vortex flow, Rev. Sci. Instrum. 76 (2005) 025110. https://doi.org/10.1063/1.1854215.

[23] G. Trenchev, S. Kolev, A. Bogaerts, A 3D model of a reverse vortex flow gliding arc reactor, Plasma Sources Sci. Technol. 25 (2016). https://doi.org/10.1088/0963-0252/25/3/035014.

[24] R.J. Azizov, A.K. Vakar, V.K. Zhivotov, M.F. Krotov, O.A. Zinov, B. V Potapkin, A.A. Rusanov, V.D. Rusanov, A.A. Fridman, The nonequilibrium plasmachemical process of decomposition of CO2 in a supersonic SHF discharge, Sov. Phys. Dokl. 28 (1983) 567–569.

[25] Y. Uytdenhouwen, K.M. Bal, I. Michielsen, E.C. Neyts, V. Meynen, P. Cool, A. Bogaerts, How process parameters and packing materials tune chemical equilibrium and kinetics in plasma-based CO2 conversion, Chem. Eng. J. (2019). https://doi.org/10.1016/j.cej.2019.05.008.

[26] M. Ramakers, G. Trenchev, S. Heijkers, W. Wang, A. Bogaerts, Gliding Arc Plasmatron: Providing an Alternative Method for Carbon Dioxide Conversion, ChemSusChem. 10 (2017) 2642–2652. https://doi.org/10.1002/cssc.201700589.

[27] R. Snoeckx, S. Heijkers, K. Van Wesenbeeck, S. Lenaerts, A. Bogaerts, CO2 conversion in a dielectric barrier discharge plasma: N2 in the mix as a helping hand or problematic impurity?, Energy Environ. Sci. (2016). https://doi.org/10.1039/c5ee03304g.

[28] B.H. Crichton, Gas discharge physics, 1996 (1996) 3–3. https://doi.org/10.1049/ic:19960997.

[29] J.L. Liu, H.W. Park, W.J. Chung, D.W. Park, High-Efficient Conversion of CO2 in AC-Pulsed Tornado Gliding Arc Plasma, Plasma Chem. Plasma Process. 36 (2016) 437–449. https://doi.org/10.1007/s11090-015-9649-2.

[30] A. Indarto, J.W. Choi, H. Lee, H.K. Song, Conversion of CO2 by gliding Arc plasma, Environ. Eng. Sci. (2006). https://doi.org/10.1089/ees.2006.23.1033.

[31] J.O. Wilkes, Introduction to COMSOL Multiphysics ( Formerly , FEMLAB ), Manual. (2009) å. http://cdn.comsol.com/documentation/5.1.0.145/IntroductionToCOMSOLMultiphysics.pdf.

[32] S. Kolev, S. Sun, G. Trenchev, W. Wang, H. Wang, A. Bogaerts, Quasi-Neutral Modeling of Gliding Arc Plasmas, Plasma Process. Polym. 14 (2017). https://doi.org/10.1002/ppap.201600110.

[33] L.C. Pitchford, L.L. Alves, K. Bartschat, S.F. Biagi, M.C. Bordage, I. Bray, C.E. Brion, M.J. Brunger, L. Campbell, A. Chachereau, B. Chaudhury, L.G. Christophorou, E. Carbone, N.A. Dyatko, C.M. Franck, D. V. Fursa, R.K. Gangwar, V. Guerra, P. Haefliger, G.J.M. Hagelaar, A. Hoesl, Y. Itikawa, I. V. Kochetov, R.P. McEachran, W.L. Morgan, A.P. Napartovich, V. Puech, M. Rabie, L. Sharma, R. Srivastava, A.D. Stauffer, J. Tennyson, J. de Urquijo, J. van Dijk, L.A. Viehland, M.C. Zammit, O. Zatsarinny, S. Pancheshnyi, LXCat: an Open-Access, Web-Based Platform for Data Needed for Modeling Low Temperature Plasmas, Plasma Process. Polym. 14 (2017) 2. https://doi.org/10.1002/ppap.201600098.

[34] N.A. Dyatko, Y.Z. Ionikh, I. V. Kochetov, D.L. Marinov, A. V. Meshchanov, A.P. Napartovich, F.B. Petrov, S.A. Starostin, Experimental and theoretical study of the transition between diffuse and contracted forms of the glow discharge in argon, J. Phys. D. Appl. Phys. 41 (2008) 055204. https://doi.org/10.1088/0022-3727/41/5/055204.

[35] G.J.M. Hagelaar, Brief documentation of BOLSIG+ version 07/2015, (2015). http://home.zcu.cz/~kozakt/MPPL/literatura/BolsigDoc0715.pdf (accessed July 18, 2019).

[36] S. Kolev, A. Bogaerts, A 2D model for a gliding arc discharge, Plasma Sources Sci. Technol. 24 (2015) 015025. https://doi.org/10.1088/0963-0252/24/1/015025.

[37] B. Weigand, J.R. Ferguson, M.E. Crawford, An extended Kays and Crawford turbulent Prandtl number model, Int. J. Heat Mass Transf. 40 (1997) 4191–4196. https://doi.org/10.1016/S0017-9310(97)00084-7.

[38] C.O. Laux, T.G. Spence, C.H. Kruger, R.N. Zare, Optical diagnostics of atmospheric pressure air plasmas, Plasma Sources Sci. Technol. 12 (2003) 125–138. https://doi.org/10.1088/0963-0252/12/2/301.

[39]    A. Berthelot, A. Bogaerts, Modeling of CO 2 Splitting in a Microwave Plasma: How to Improve the Conversion and Energy Efficiency, J. Phys. Chem. C. 121 (2017) 8236–8251. https://doi.org/10.1021/acs.jpcc.6b12840.

[40]    S. Heijkers, A. Bogaerts, CO2 Conversion in a Gliding Arc Plasmatron: Elucidating the Chemistry through Kinetic Modeling, J. Phys. Chem. C. (2017). https://doi.org/10.1021/acs.jpcc.7b06524.

[41]    J. Cheng, L. Du, W. Xiang, Incompressible Jet Flows in a de Laval Nozzle with Smooth Detachment, Arch. Ration. Mech. Anal. 232 (2019) 1031–1072.